CivilEng

MDPI

Article

Load-Carrying Capacity and Cracking Behavior of Concrete Pipes Reinforced with Recycled GFRP Fibers and GFRP Bars

Shuaiyuan Wang [1], Jianzhong Chen [1], Yong Lv [1,*], Pengfei Song [2] and Mingqing Sun [1]

[1] Hubei Key Laboratory of Theory and Application of New Materials, School of Physics and Mechanics, Wuhan University of Technology, Wuhan 430070, China; 18303745362@163.com (S.W.); cjzwhut@163.com (J.C.); sunmqing@whut.edu.cn (M.S.)
[2] Hengrun Group New Materials Co., Ltd., Hengshui 053100, China; ppsonl@126.com
* Correspondence: lvyonghl@whut.edu.cn; Tel.: +86-134-6998-8526

Abstract

Three-edge bearing (TEB) tests and a crack-width-dependent load-carrying model were used to assess the combined effects of recycled glass fiber-reinforced polymer (rGFRP) short fibers and glass fiber-reinforced polymer (GFRP) bars in concrete pipes. Using the force method, a circumferential statically indeterminate ring analysis was formulated to obtain internal forces at critical sections and the neutral-axis position. Fiber distribution was simulated by means of Monte Carlo sampling, and single-filament pull-out tests were fitted to relate embedded length to pull-out force, enabling calculation of the fiber-bridging contribution at cracked sections. Ten specimen types with different bar/fiber schemes were tested under external pressure to validate the model. Predicted cracking and ultimate loads agreed with measurements, with most errors within ±20%. Adding 1% (vol.) rGFRP fibers increased the cracking load by 11.81% and the ultimate load by 0.45%. Without fibers, replacing steel bars with equal-area GFRP bars increased the cracking load by 1.35% but reduced the ultimate load by 35.45%. For all specimens, the load–maximum crack-width relation was strongly linear ($R^2 > 0.93$). The proposed approach and dataset support engineering use of recycled GFRP materials for crack control and load-carrying design of concrete pipes.

Keywords: recycled GFRP fibers; GFRP bars; concrete pipes; three-edge bearing (TEB)

1. Introduction

Fiber-reinforced polymer (FRP) composites are materials in which fibers and their products serve as reinforcement and synthetic resins act as the matrix [1]. Owing to their high specific strength, corrosion resistance, light weight, and design flexibility, FRP composites have been widely used in civil engineering, transportation, electrical equipment, aerospace, and wind-energy systems [2,3]. With the rapid expansion of these applications, especially the large-scale use of thermoset glass-fiber-reinforced polymer (GFRP) in wind-turbine blades, the disposal of end-of-life composite products has become an increasingly important environmental issue. Because most of these materials are non-biodegradable and difficult to remanufacture once cured, their continued accumulation may impose considerable long-term environmental burdens if effective recycling routes are not developed [4].

Among the available treatment options for waste composites, mechanical recycling is generally regarded as one of the most economical and industrially feasible routes. It is

Academic Editors: Akanshu Sharma and Angelo Luongo

Received: 13 February 2026
Revised: 12 March 2026
Accepted: 28 March 2026
Published: 1 April 2026

currently the most widely used commercial recycling technology for glass- and carbon-fiber composites, exhibits relatively low energy consumption compared with other recycling methods, and can effectively reduce the environmental risks associated with retired wind-turbine blades and other composite wastes [5–7]. However, the practical value of mechanically recycled GFRP depends strongly on how it can be reused in downstream applications. In recent years, cement-based materials have been considered a promising outlet because they can consume large volumes of recycled composite waste while also benefiting from the filling and crack-bridging effects of recycled fibers and powders.

Existing studies have shown that the influence of rGFRP on cementitious materials is closely related to the morphology, particle size, fiber length, dosage, and replacement mode of the recyclate. Farinha [8], Zhou [9], and Bu [10] incorporated recycled GFRP into mortar or cement paste systems and reported improvements in mechanical performance under suitable conditions. Ribeiro [11] added rGFRP to precast concrete blocks and observed enhanced properties; Asokan [12] used GFRP waste as a partial replacement for fine aggregate and found improvements in both mechanical and durability performance; and Garcia [13] further demonstrated that recycled GFRP can act as short-fiber reinforcement and significantly increase the flexural and compressive strengths of microconcrete. At the same time, other studies have noted that excessive replacement ratios or unsuitable recycled forms may reduce workability and even deteriorate hardened properties [14–19]. These findings suggest that recycled FRP should not be regarded as a uniform material, but rather as a family of recycled constituents with different reinforcing and filling roles depending on their geometry and load-transfer characteristics. Overall, rGFRP has shown clear potential in concrete, especially for crack control and post-cracking resistance, but its effectiveness still needs to be evaluated in relation to specific structural forms and loading conditions.

This issue is particularly relevant to concrete pipe structures. Concrete pipes are widely used for the conveyance of water, sewage, oil, and other fluids, and they usually operate in buried environments where load-carrying capacity, serviceability, and durability are all critical. In conventional reinforced concrete pipes, circumferential reinforcement is typically used to enhance bending resistance; however, steel corrosion remains a key concern in long-term service, especially when cracks allow moisture, chloride ions, or aggressive substances in wastewater to reach the reinforcement [20]. Once corrosion initiates, crack propagation, stiffness degradation, and durability loss may accelerate. Therefore, replacing steel reinforcement with corrosion-resistant GFRP bars offers an attractive alternative for pipe structures exposed to aggressive environments.

Against this background, the structural use of GFRP bars in concrete has received extensive attention. Compared with steel reinforcement, GFRP bars exhibit excellent corrosion resistance and high tensile strength, but they also possess distinctive mechanical characteristics, including a lower elastic modulus, an almost linear-elastic response up to rupture, and bond behavior that depends strongly on surface treatment. These characteristics mean that GFRP-reinforced concrete members often face more demanding serviceability issues, particularly in terms of crack width and deflection control. Shabani [21] showed that fiber incorporation can improve the flexural and serviceability response of GFRP-reinforced concrete beams. Bui [22] found that the equivalent reinforcement ratio and FRP bar type significantly affect the load-carrying capacity and deformation performance of reinforced concrete beams. Sun [23,24] further reported that hybrid-reinforced concrete beams and FRP-reinforced concrete beams can provide favorable corrosion resistance together with competitive structural performance. Other studies have also emphasized the importance of bond characteristics and reinforcement configuration in determining crack development, stiffness variation, and failure mode in GFRP-reinforced members [25–28]. These results indicate that although GFRP bars are promising substitutes for steel, their application in

concrete structures must be accompanied by careful evaluation of cracking behavior and service performance.

For concrete pipes, such concerns are even more critical because crack width directly affects leakage resistance, durability, and serviceability assessment under external loading. Existing studies on the TEB behavior of concrete pipes have mainly focused on conventional reinforced concrete pipes, steel-fiber-reinforced concrete pipes, and synthetic-fiber-reinforced concrete pipes. These studies have shown that fiber addition can improve crack distribution, toughness, and load-carrying performance, and that pipe diameter, reinforcement form, and material composition all affect the response of pipes under external load [29–31]. Nevertheless, most available research still centers on traditional reinforcement systems or single-fiber modification. Studies on concrete pipes simultaneously reinforced with GFRP bars and recycled rGFRP fibers remain very limited, especially under TEB conditions where circumferential bending governs the structural response.

This study investigates the load-carrying and cracking behavior of concrete pipes reinforced with rGFRP fibers and GFRP bars under TEB conditions. At the cracked section, a fiber-bridging characterization approach is introduced with crack width as the core variable; combined with Monte Carlo random distribution and single-filament pull-out test fitting, the "bond-slip-pull-out" contribution of fibers is quantified. On this basis, TEB tests on specimens with different reinforcement types and fiber dosages are conducted to validate the model, clarify the inhibition effect of rGFRP fibers on crack initiation and propagation, and reveal the mechanisms governing differences in crack control and ultimate capacity when GFRP bars replace steel bars. The results provide experimental data and theoretical support for crack-resistant design and capacity prediction of concrete pipes using recycled GFRP materials.

2. Method for Calculating TEB Load-Carrying Capacity Considering Crack Width and Fiber Bridging

In the structural performance evaluation of concrete drainage pipes, the three-edge bearing (TEB) test is an internationally recognized standard loading method (e.g., ASTM C497 [32] and GB/T 11836 [33]). Under the boundary condition of a crown line load with two side supports, this test reasonably simulates the typical circumferential stress state of pipes subjected to backfill soil pressure, surface concentrated loads, or uneven foundation reactions. Under TEB loading, the pipe primarily behaves as a ring structure in which bending moments dominate, accompanied by a certain axial-force effect. Tensile stress concentrations generally develop at the crown and invert, as well as in the vicinity of the supports, leading to a progressive failure process characterized by the elastic stage, cracking stage, stable crack propagation stage, and ultimate capacity stage. In engineering design and durability assessment, pipes are often governed not only by material strength but also by serviceability indicators such as crack width, deflection, and crack growth rate. Therefore, traditional simplifications, such as equating cracking with failure or neglecting post-cracking tensile contributions, are insufficient to accurately characterize the actual load-carrying and deformation behavior of reinforced and fiber-composite pipe systems under TEB conditions.

2.1. Theoretical Modeling and Basic Assumptions

To balance computational tractability and engineering applicability, the following assumptions are adopted:

1. Deformation compatibility and small-deformation assumption

Under TEB loading, the pipe is assumed to satisfy the small-deformation condition, and the influence of geometric nonlinearity on internal-force redistribution is neglected.

The circumferential section is further assumed to remain plane, which facilitates the establishment of flexibility coefficients and compatibility equations based on the virtual work method.

2. Stage-wise load-sharing assumption

Elastic stage (uncracked): Concrete, GFRP bars, and fibers are assumed to deform compatibly. Because short fibers primarily function through interfacial bonding, their contribution to the global stiffness may be represented by an equivalent stiffness in the internal-force analysis or considered separately in the sectional capacity calculation.

Post-cracking stage: The tensile concrete is assumed to cease carrying load, and the stress in the tensile-zone concrete is neglected. The sectional tensile force is resisted by the tensile force in the GFRP (or steel) bars together with the fiber-bridging tensile force across the crack plane. The compression zone is carried by concrete and is simplified using an equivalent stress block.

3. Linear elasticity and failure criterion assumption

When establishing the flexibility coefficients in the force-method formulation, the materials are assumed to behave linearly elastically prior to failure, consistent with the basis of the virtual displacement calculation. The ultimate limit state is assumed to be governed by either crushing of the concrete in the compression zone or rupture of the GFRP bars.

Applicability: This method is applicable to reinforced concrete or FRP-reinforced concrete pipes whose geometry and loading conform to the standard TEB configuration, particularly for pipes containing short fibers, in which crack width and fiber-bridging effects need to be explicitly considered. It is not applicable to cases involving severe local indentation, pronounced slip, impact or dynamic effects. It is not applicable to cases with severe local indentation, pronounced slip, or impact/dynamic effects.

Under TEB conditions, a rigid loading beam applies a vertical concentrated load at the crown, while two parallel support beams provide reactions at the bottom sides, forming a typical "top load–bottom supports" configuration, as shown in Figure 1a. Because the loading and support conditions are symmetric with respect to the vertical mid-plane, and the pipe behaves as an axisymmetric ring, the circumferential internal-force distribution is also symmetric.

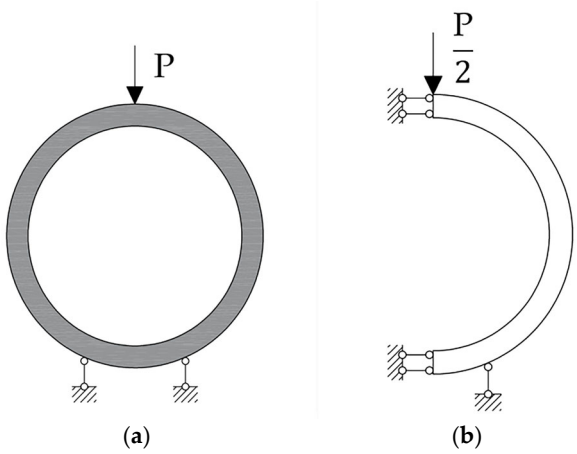

Figure 1. Loading configuration and force equilibrium of the pipe: (**a**) Loading configuration and force equilibrium of the pipe under TEB; (**b**) Symmetry-reduced loading configuration and force equilibrium.

For simplification, only a semi-ring is modeled, as shown in Figure 1b, and the cut at the axis of symmetry is treated as a statically indeterminate system with two redundant

constraints. For statically indeterminate structures, the redundant forces can be solved using either the force method or the displacement method. In this study, the force method in structural mechanics is adopted. Specifically, the compatibility equations are formulated in the form of a "basic structure + redundant forces" system, and the flexibility coefficients are determined using the unit-load method to solve for the redundant forces and recover the actual internal forces in the closed ring.

This simplification preserves the essential boundary conditions and the statically indeterminate nature of the TEB "top load–bottom supports" configuration, thereby enabling effective evaluation of the bending moment and axial force distributions at critical sections, such as the crown, invert, and regions near the supports.

2.2. Pull-Out Force Model for rGFRP Fibers

The bridging force provided by an individual fiber is related to its effective embedded (bond) length, as expressed in Equation (1). To establish the relationship between bond force and embedded length, the single-filament pull-out test shown in Figure 2a was conducted, and the corresponding experimental results are presented in Figure 2b. It can be seen that the force carried by a short fiber is approximately linearly correlated with its embedded length, which is consistent with the trend indicated by Equation (1). Therefore, a linear function is adopted to fit the single-filament pull-out test data, thereby completing the expression for calculating bond force as a function of embedded length.

$$F(L_a) = a_e \tau_f = \pi d_f L_a \tau_f \quad (1)$$

where a_e denotes the bond area between the rGFRP fibers and concrete, and τ_f represents the interfacial bond strength between the rGFRP fibers and the concrete matrix.

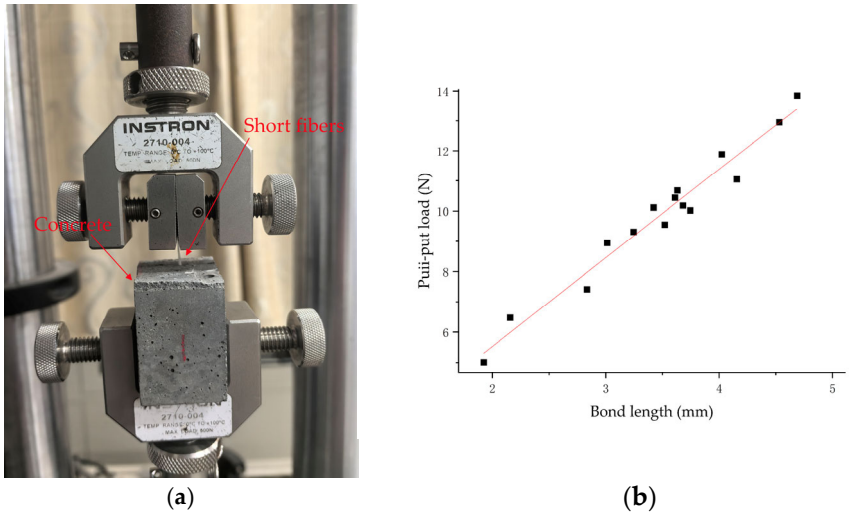

(**a**) (**b**)

Figure 2. Single-filament pull-out test: (**a**) Configuration of the single-filament pull-out test; (**b**) Results of the single-filament pull-out test and curve fitting.

2.3. Internal Force Analysis of the Ring Structure

According to the force method in structural mechanics, for an n-degree statically indeterminate structure, it is necessary to establish n deformation compatibility equations to solve for the redundant unknown forces. It is assumed that concrete, rGFRP fibers and GFRP bars all remain in the linear elastic deformation stage prior to failure, and their stress-strain relationship conforms to Hooke's law. This assumption provides the basis for the virtual displacement calculation. In this paper, the unit-load method is adopted to

determine the flexibility coefficients. The unknown forces are denoted as X_1 and X_2, as shown in Figure 3.

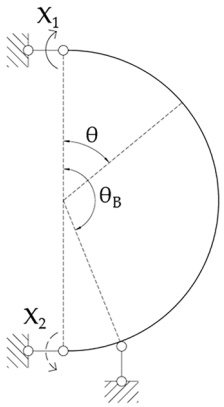

Figure 3. Force equilibrium diagram after substitution using the force method. Where θ is the angle between the radial line at the calculation position and the radial line of the loading beam, and θ_B is the angle between the radial line of the supporting beam and the radial line of the loading beam.

Based on Zhang's derivation [34], the unknown forces is

$$\begin{cases} X_1 = B_1 \frac{PR}{2} \\ X_2 = B_2 \frac{PR}{2} \end{cases} \tag{2}$$

where the coefficients

$$\begin{cases} B_1 = \frac{2(C_2 - 3C_1)}{\pi} \\ B_2 = \frac{2(C_1 - 3C_2)}{\pi} \end{cases} \tag{3}$$

Once the unknown forces are determined, the internal forces of the closed ring structure under TEB loading can be obtained, as shown in Equation (4):

$$\begin{cases} M(\theta) = M_1(\theta)X_1 + M_2(\theta)X_2 + M_P(\theta) \\ N(\theta) = N_1(\theta)X_1 + N_2(\theta)X_2 + N_P(\theta) \\ Q(\theta) = Q_1(\theta)X_1 + Q_2(\theta)X_2 + Q_P(\theta) \end{cases} \tag{4}$$

where $M_i, N_i, Q_i (i = 1, 2)$ represent the internal forces in the tube wall when only $X_i (i = 1, 2)$ acts on the primary structure; M_P, N_P, Q_P represent the internal forces in the tube wall when only $F_P = P/2$ acts on the primary structure, as shown in Equation (5):

$$M_1(\theta) = \tfrac{1+\cos\theta}{2},\ 0 \le \theta \le \pi \qquad M_P(\theta) = \begin{cases} \frac{PR}{4}\sin\theta_B(1-\cos\theta) - \frac{PR}{2}\sin\theta, & 0 \le \theta \le \theta_B \\ -\frac{PR}{4}\sin\theta_B(1+\cos\theta), & \theta_B \le \theta \le \pi \end{cases}$$

$$N_1(\theta) = -\tfrac{\cos\theta}{2R},\ 0 \le \theta \le \pi$$

$$Q_1(\theta) = \tfrac{\sin\theta}{2R},\ 0 \le \theta \le \pi \qquad N_P(\theta) = \begin{cases} \frac{P}{4}\sin\theta_B\cos\theta + \frac{P}{2}\sin\theta, & 0 \le \theta \le \theta_B \\ \frac{P}{4}\sin\theta_B\cos\theta, & \theta_B \le \theta \le \pi \end{cases} \tag{5}$$

$$M_2(\theta) = \tfrac{1-\cos\theta}{2},\ 0 \le \theta \le \pi$$

$$N_2(\theta) = \tfrac{\cos\theta}{2R},\ 0 \le \theta \le \pi \qquad Q_P(\theta) = \begin{cases} \frac{P}{2}\cos\theta - \frac{P}{4}\sin\theta_B\sin\theta, & 0 \le \theta \le \theta_B \\ -\frac{P}{4}\sin\theta_B\sin\theta, & \theta_B \le \theta \le \pi \end{cases}$$

$$Q_2(\theta) = -\tfrac{\sin\theta}{2R},\ 0 \le \theta \le \pi;$$

2.4. Sectional Load-Carrying Capacity Calculation

The sectional forces of the concrete pipe are assumed to consist of the following components: the concrete compressive resultant, represented using the equivalent rectangular

stress block specified in ACI 318 [35]; the tensile force provided by the circumferential reinforcement, treated as a concentrated force; and the tensile force provided by the short fibers, taken as the resultant of all short fibers. In particular, for concrete containing rGFRP short fibers, the fiber-bridging force at the cracked section cannot be neglected.

Based on the sectional force diagram of the pipe shown in Figure 4, the mechanical equilibrium equations are established, as shown in Equation (6):

$$\begin{cases} N = 0.85 f_c a l - A_s f_y - N_f \\ M = A_s f_y \left(d - \frac{a}{2}\right) + M_f \end{cases} \tag{6}$$

where N_f is the sum of the tensile forces provided by all short fibers, and M_f is the sum of the moments provided by all short fibers about the centroid of the concrete compression zone.

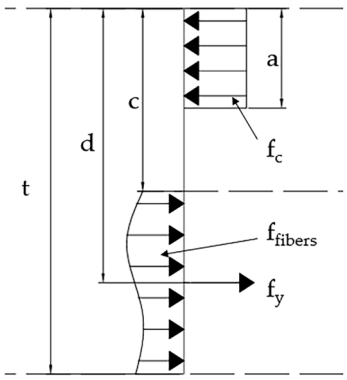

Figure 4. Force equilibrium diagram of the pipe cross-section. Where a is the height of the concrete compression zone, f_y is the stress in the circumferential reinforcement, f_{fibers} is the tensile force provided by the short fibers, f_c is the compressive stress in the concrete, t is the thickness of the concrete pipe, d is the distance from the centroid of the circumferential reinforcement to the outer pipe wall.

2.5. Short-Fiber Force Calculation Considering Crack Width

The key to quantifying the fiber-bridging force is the introduction of crack width into the sectional equilibrium analysis. After cracking, the short fibers spanning the crack plane generate pull-out resistance through interfacial bonding, thereby forming a bridging tensile force. To capture the controlling effect of crack width on the bridging force, the following equivalent description is adopted:

The crack is idealized as a planar state without local warping, with a maximum opening ω_m, and the crack width is assumed to vary linearly along the depth direction. The tensile stress of concrete in the crack zone is neglected, as shown in Figure 5.

The crack width is assumed to vary approximately linearly along the crack depth, as follows:

$$\frac{\omega}{\omega_m} = \frac{x}{L_\omega} \tag{7}$$

Due to the randomness of fiber position, orientation, and bond length, the Monte Carlo random sampling method is adopted to generate N fibers crossing the crack plane. The bridging contribution of each fiber is calculated individually, and the resultant axial force N_f and moment contribution M_f are obtained by summing the contributions of all fibers.

$$\begin{cases} N_f = \sum_{1}^{N} F[L_a(i)] \sin[\theta(i)] \\ M_f = \sum_{1}^{N} F[L_a(i)] \sin[\theta(i)][L_\omega(i) - x(i)] \end{cases} \tag{8}$$

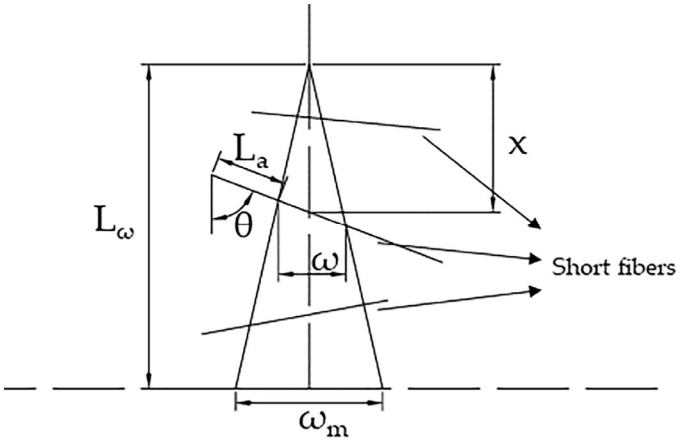

Figure 5. Force equilibrium diagram of short fibers considering crack width effects. Where x is the position coordinate of the short fiber, ω is the crack width at the location of the short fiber, L_ω is the crack depth, ω_m is the maximum crack width, and θ is the angle between the short fiber and the crack plane.

The position and bond length of the short fibers are assumed to be random. According to the actual distribution characteristics, in the Monte Carlo random sampling procedure, the position coordinate x of the short fibers is assumed to be uniformly distributed over $(0, L_\omega)$, and the bond length L_a is uniformly distributed over $(0, L/2 - \omega/2)$.

The orientations of the short fibers are randomly distributed in three-dimensional space. Accordingly, the probability density function of the angle θ between the short fibers and the crack plane is given as follows:

$$P(\theta) = \sin\theta, \theta \in \left(0, \frac{\pi}{2}\right) \tag{9}$$

The fiber number N is determined using the calculation method for the number of fibers on a concrete cross-section proposed by Zhao [36]:

$$N = \eta \frac{VV_f}{L_c \alpha_f} \tag{10}$$

where $\eta = 0.42$ is the fiber orientation coefficient, V is the volume of the concrete pipe, V_f is the fiber volume fraction, L_c is the side length of the specimen perpendicular to the cross-section, and α_f is the cross-sectional area of the rGFRP short fibers, calculated by Equation (11).

$$\alpha_f = \pi d_f^2 \tag{11}$$

where d_f is the diameter of the rGFRP short fibers.

2.6. Section Summary

This section proposes a calculation method for the TEB load-carrying capacity that accounts for crack width and the bridging effect of rGFRP short fibers. At the control section, an equilibrium framework consisting of the equivalent concrete compression stress block, the tensile force of the main reinforcement, and the tensile force provided by fiber bridging is established. Combined with single-filament pull-out tests and Monte Carlo simulations, the contribution of fiber bridging is quantitatively evaluated. This framework provides the basis for the subsequent experimental comparison and parameter determination.

3. Specimens and Test Program

3.1. Specimen Design and Materials

To systematically evaluate the synergistic and individual effects of rGFRP short fibers and GFRP bars on the mechanical performance of concrete drainage pipes, four categories of comparative specimens were designed, with two replicates in each category, resulting in a total of eight concrete pipe specimens. All specimens were designed, fabricated, and cured in strict accordance with the national standard GB/T 11836-2023, Concrete and reinforced concrete drainage pipes [33], to ensure the standardization and comparability of the test results.

The geometric parameters of the large-diameter specimens were uniformly specified as follows: length of 2000 mm, outer diameter of 600 mm, and wall thickness of 100 mm, thereby forming a standard ring section. The concrete matrix consisted of concrete with a specified cube compressive strength of 40 MPa, and the mix proportion was optimized through laboratory trial mixes.

For the reinforcement layout, 12 longitudinal distribution bars with a diameter of 6 mm were uniformly arranged along the circumference, as shown in Figure 6. The circumferential load-carrying reinforcement consisted of 28 closed rings with a diameter of 6 mm and a spacing of approximately 70 mm. Two types of main reinforcement were used: HRB400 hot-rolled ribbed steel bars and GFRP bars, both provided with spiral ribs to enhance mechanical interlock with the concrete. The nominal cross-sectional areas of the two types of bars were identical, ensuring the same reinforcement ratio. For both the steel-bar and GFRP-bar specimens, the longitudinal and circumferential bars were tied together using steel wire.

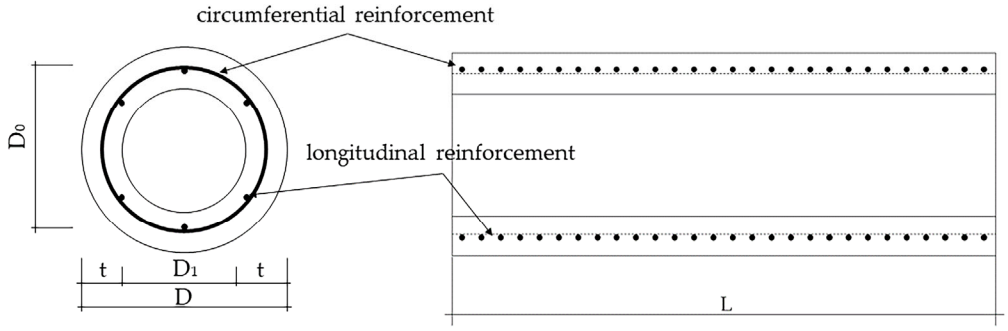

Figure 6. Geometry and reinforcement layout of the pipe.

In the figure, D_0 denotes the position of the circumferential reinforcement, and L denotes the pipe length.

The geometric parameters of the small-diameter specimens were uniformly specified as follows: length of 300 mm, outer diameter of 380 mm, and inner diameter of 315 mm, thereby forming a standard ring section. The concrete matrix consisted of concrete with a specified cube compressive strength of 40 MPa, and the mix proportion was optimized through laboratory trial mixes.

The rGFRP short fibers were produced from waste wind-turbine blades through cutting, crushing, and screening. The fibers had a length of 6 mm and a nominal diameter of approximately 0.5 mm, with an irregular flat shape. The fibers were incorporated into the concrete mixture at a volume fraction of 1%. To ensure uniform dispersion, a "dry mixing followed by wet mixing" procedure was adopted: cement, sand, aggregate, and fibers were first dry-mixed for 3 min, after which water and superplasticizer were added and wet-mixed for 4 min until no obvious fiber agglomeration was observed.

The specimen IDs and key parameters are listed in Table 1.

Table 1. Specimen identification and key parameters.

Label	Outer Diameter (mm)	Inner Diameter (mm)	Reinforcement Type	Number of Circumferential Reinforcement Rings	Circumferential Reinforcement Ratio (%)	Recycled Fiber Volume Content (%)
D1-B28-0	1200	1000	Steel Bars	28	0.704	0
D1-B28-1	1200	1000	Steel Bars	28	0.704	1
D1-C28-0	1200	1000	GFRP Bars	28	0.704	0
D1-C28-1	1200	1000	GFRP Bars	28	0.704	1
D2-B2	380	315	Steel Bars	2	0.580	0
D2-B3	380	315	Steel Bars	3	0.870	0
D2-B4	380	315	Steel Bars	4	1.160	0
D2-C2	380	315	GFRP Bars	2	0.580	0
D2-C3	380	315	GFRP Bars	3	0.870	0
D2-C4	380	315	GFRP Bars	4	1.160	0

All specimens were cast in steel molds and compacted using an internal vibrator. After 24 h, the specimens were demolded and cured for 28 days in a standard curing room at 20 ± 2 °C and a relative humidity of at least 95%. They were then stored in the laboratory environment for 7 days at 23 ± 2 °C and a relative humidity of 50% to stabilize their moisture content prior to the loading tests.

3.2. Loading Setup for External Pressure Tests

The TEB loading device compliant with GB/T 11836 was used, as shown in Figure 7a. For the large-diameter pipes (Series D1), the loading system consisted of a 60-ton hydraulic jack, a high-precision load sensor, a data acquisition system, and a rigid distribution beam. A 10 mm thick natural rubber pad was placed between the loading beam and the specimen crown to simulate a compliant bedding layer in practice and to avoid stress concentration. The two bottom support beams were 150 mm × 150 mm timber blocks with leveled surfaces, and their lateral positions were restrained using steel limit frames to prevent rolling or sliding.

(**a**) (**b**)

Figure 7. Test setup (**a**) Test setup for the large-diameter pipe; (**b**) Test setup for the small-diameter pipe.

For the small-diameter pipes (Series D2), a loading setup geometrically similar to that used for Series D1 was adopted, as shown in Figure 7b. The load was applied and measured using an electronic universal testing machine. A 10 mm thick natural rubber pad was also placed at the crown contact. The two bottom support beams were replaced with

engineering plastic blocks to facilitate direct drilling and fixation to the base of the testing machine, while restraining both axial and radial displacements.

3.3. Theoretical Estimation of Loading Levels and Loading Protocol

To ensure test safety and accurately capture the key performance indicators, namely the cracking load and the ultimate load, a strategy combining theoretical estimation with staged loading was adopted. First, based on the theoretical model presented in Section 1, the cracking moment and ultimate moment of each specimen were calculated and then converted into the corresponding theoretical cracking load and theoretical ultimate load using the geometric relationship of the TEB test, in which the moment is linearly related to the applied load.

The loading protocol consisted of two stages:

1. Cracking load determination:

The load was first increased at a constant rate to 80% of the theoretical cracking load and held for 1 min to inspect the specimen for cracks. A handheld crack-width gauge was used to determine whether the crack width exceeded the allowable limit. The load was then increased in increments of 10% of the cracking load up to the theoretical cracking load, during which crack initiation was observed and the corresponding crack widths were measured and recorded. Thereafter, loading continued in increments of 5% of the cracking load until the crack width exceeded the allowable limit, and the crack width at each load level was measured and recorded. The allowable crack widths are listed in Table 2.

Table 2. Allowable crack width for concrete pipes.

Pipe Type	Reinforced Concrete Pipe	GFRP Reinforced Concrete Pipe
Allowable crack width (mm)	0.2	0.5

2. Ultimate load determination:

The load was first increased at a constant rate to 80% of the theoretical ultimate load and held for 1 min to verify whether failure had occurred. The load was then increased in increments of 10% of the theoretical ultimate load up to the predicted ultimate load, while the specimen response was continuously monitored. Subsequently, loading continued in increments of 5% of the theoretical ultimate load until the peak load was reached. Loading was maintained briefly after the peak load to confirm that no higher load could be attained. Therefore, the failure load reported in this study was defined as the peak load.

The entire loading process strictly followed the principle of "slow loading, stepwise increments, observation, and recording" to ensure data reliability and test repeatability.

4. Experimental Investigation of Pipe Load-Carrying Capacity

4.1. Analysis of Experimental Observations

Under TEB external-pressure loading, the response of all concrete pipe specimens exhibited a typical three-stage behavior, as shown in Figure 8: elastic stage, stable crack propagation stage, failure stage.

In the elastic stage (load < cracking load), the structure remained in a linearly elastic state, and no visible cracks were detected either by visual inspection or by measurement instruments. During this stage, the tensile stress was primarily carried by the concrete matrix, while the GFRP bars or steel bars were not yet significantly engaged.

When the load approached the theoretical cracking load, the tensile strength of the concrete at the invert was exceeded, and the first axial microcrack initiated on the inner surface of the invert, with a width typically smaller than 0.05 mm. This event marks

the onset of cracking and indicates that the structure has entered a cracked service state. Notably, the specimens containing rGFRP short fibers (D1-B28-1 and D1-C28-1) generally exhibited higher crack-initiation loads as well as finer and denser initial cracks, indicating that the fibers effectively inhibited the rapid coalescence of microcracks.

(**a**) (**b**) (**c**)

Figure 8. Characteristic response of the pipe at different stages under TEB loading (**a**) elastic stage; (**b**) stable crack propagation stage; (**c**) failure stage.

After entering the crack-propagation stage, as the load continued to increase, existing cracks gradually extended along the pipe-wall thickness and induced new cracks in adjacent regions. The number of cracks continuously increased, and the maximum crack width also developed gradually. In the initial part of this stage, the tensile resistance of the member was still mainly carried by the concrete. However, when the load increased to a certain level, the concrete could no longer effectively resist tension, and the tensile force was transferred to the reinforcement. Because the tests were conducted under displacement-controlled loading, this transition in the load-carrying mechanism was reflected in the load–displacement curve as an instantaneous drop in load. By comparison, since the elastic modulus of GFRP bars is only about one quarter of that of steel bars, the GFRP-bar specimens (Series C) exhibited a more pronounced load drop during this transition.

In the final failure stage, that is, between the cracking load and the failure load, the load-carrying capacity of the specimens generally showed a trend of first increasing and then gradually stabilizing, with a pronounced plateau stage, as shown in Figure 9.

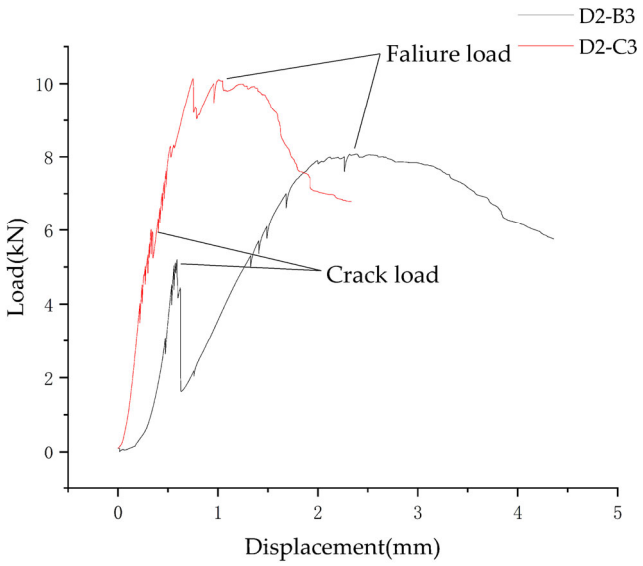

Figure 9. Load–displacement curves of typical specimens.

This plateau stage could persist for a certain period even after the failure load was reached, after which the load-carrying capacity gradually decreased, exhibiting a softening response. By comparison, reinforced concrete pipes showed a faster post-failure softening process and a more pronounced decline in load-carrying capacity, whereas GFRP-reinforced concrete pipes were able to retain their subsequent load-carrying capacity to a greater extent.

Finally, the specimen exhibited evident cracking, and its load-carrying capacity decreased significantly, as shown in Figure 10.

(**a**) (**b**)

Figure 10. Final cracking and failure pattern of the specimen (**a**) Left view; (**b**) Right view.

Overall, the incorporation of rGFRP short fibers effectively delayed crack development and improved the structural ductility. Although GFRP bars provide superior corrosion resistance, their relatively low elastic modulus results in larger deformation, wider cracks, and a more brittle failure mode. Therefore, their use should be approached with caution in applications with stringent deformation-control requirements.

4.2. Test Results

To verify the validity of the proposed model, the calculated cracking load P_{cr}^{cal} and calculated ultimate load P_u^{cal}, obtained using the above method, are compared with the experimentally measured values $P_{cr}^{\exp}$ and $P_u^{\exp}$. The error is calculated as shown in Equation (12):

$$Error = \frac{P^{cal} - P^{\exp}}{P^{\exp}} \times 100\% \quad (12)$$

As summarized in Table 3, the predicted cracking and ultimate loads agree well with the experimental results overall, with an average absolute error of 14.37%. This indicates that the proposed model can reasonably predict the cracking and ultimate load levels within an engineeringly acceptable range.

A comparison between the theoretical predictions and the experimental results shows that the errors for all specimens were within ±30%, and that the majority were within ±20%, confirming the good predictive capability of the model for most loading cases. Nevertheless, some unavoidable discrepancies remain, mainly because the theoretical model is based on a linear-elastic assumption in the internal-force analysis, together with several other assumptions and simplifications. These idealized treatments inevitably lead to a certain degree of deviation between the theoretical predictions and the experimental results.

It should also be emphasized that the present study is based on the standardized TEB loading condition and does not explicitly consider the interaction between the pipe and the surrounding ground. In actual buried service, soil stiffness, bedding support, backfill compaction, and nonuniform ground reactions may affect load redistribution and crack development, and may either alleviate or aggravate local stresses at the crown, invert, and

support regions. Consequently, the cracking and ultimate loads obtained in the TEB test should be interpreted as standardized structural performance indicators under controlled boundary conditions, rather than direct in-situ capacities for all burial environments.

Table 3. Comparison of Experimental and Theoretical Cracking Loads and Failure Loads of Specimens.

Label	Calculated Cracking Load (kN/m)	Measured Cracking Load (kN/m)	Cracking Load Error (%)	Calculated Failure Load (kN/m)	Measured Failure Load (kN/m)	Failure Load Error (%)
D1-B28-0	30.08 30.08	32.67 35.5	8.61 18.02	62.47 62.47	63.73 73.17	2.02 17.13
D1-B28-1	36.05 36.05	37.68 39.43	4.52 9.38	75.08 75.08	52.87 67.98	−29.58 −9.46
D1-C28-0	29.42 29.42	35.5 34.4	20.67 16.93	48.07 48.07	35.5 42.15	−26.15 −12.32
D1-C28-1	34.08 34.08	40.13 37.11	17.75 8.89	50.83 50.83	45.28 42.18	−10.92 −17.02
D2-B2	5.83	7.02	16.95	8.16	7.10	−14.99
D2-B3	6.21	7.62	18.50	11.01	10.01	−9.98
D2-B4	6.39	8.01	20.25	13.07	11.73	−11.38
D2-C2	4.54	5.73	20.80	7.47	7.02	−6.45
D2-C3	6.10	6.32	3.43	9.66	8.03	−20.27
D2-C4	6.95	7.31	4.95	11.53	9.23	−24.92

To quantitatively describe crack development in concrete pipes after cracking, typical specimens (D1-B28-0-1, D1-B28-1-2, D1-C28-0-2, D1-C28-1-2) were selected to analyze the relationship between the maximum crack width ω_{max} and the load P recorded during external pressure loading, as shown in Figure 11. The maximum crack width was defined as the maximum value among all crack-gauge readings at the same load level, representing the most unfavorable crack-control state. Overall, the crack width remained essentially zero before the first crack appeared. Once the initial crack formed, the crack width increased rapidly, and the specimen entered a stable crack-propagation stage, during which the crack width continued to increase with the external-pressure load.

It can be seen from Figure 11 that the relationship between the post-cracking load-maximum crack width exhibits an approximately linear characteristic within the selected load range. Therefore, a linear model is adopted for fitting:

$$\omega_{max} = aP + b \tag{13}$$

where a can be interpreted as the crack propagation rate, namely the increment in maximum crack width caused by a 1-kN increase in load, and b is related to the cracking threshold, the nonlinear effects in the initial crack propagation stage, and other influencing factors.

Figure 11 presents the load–maximum crack width curves of the typical specimens. It can be seen that all curves increase approximately linearly after cracking, indicating that, within the service load range, the crack width exhibits a good linear relationship with the external load. This characteristic makes it possible to back-calculate the load level from the crack width.

Least-squares linear regression of the four representative specimens produced high goodness-of-fit values of 0.98, 0.96, 0.93, and 0.96, respectively. These results indicate that, during the stable post-cracking stage, the maximum crack width is strongly linearly correlated with the external pressure load, and that a simplified linear relationship can therefore be used for engineering description and comparative evaluation of crack development.

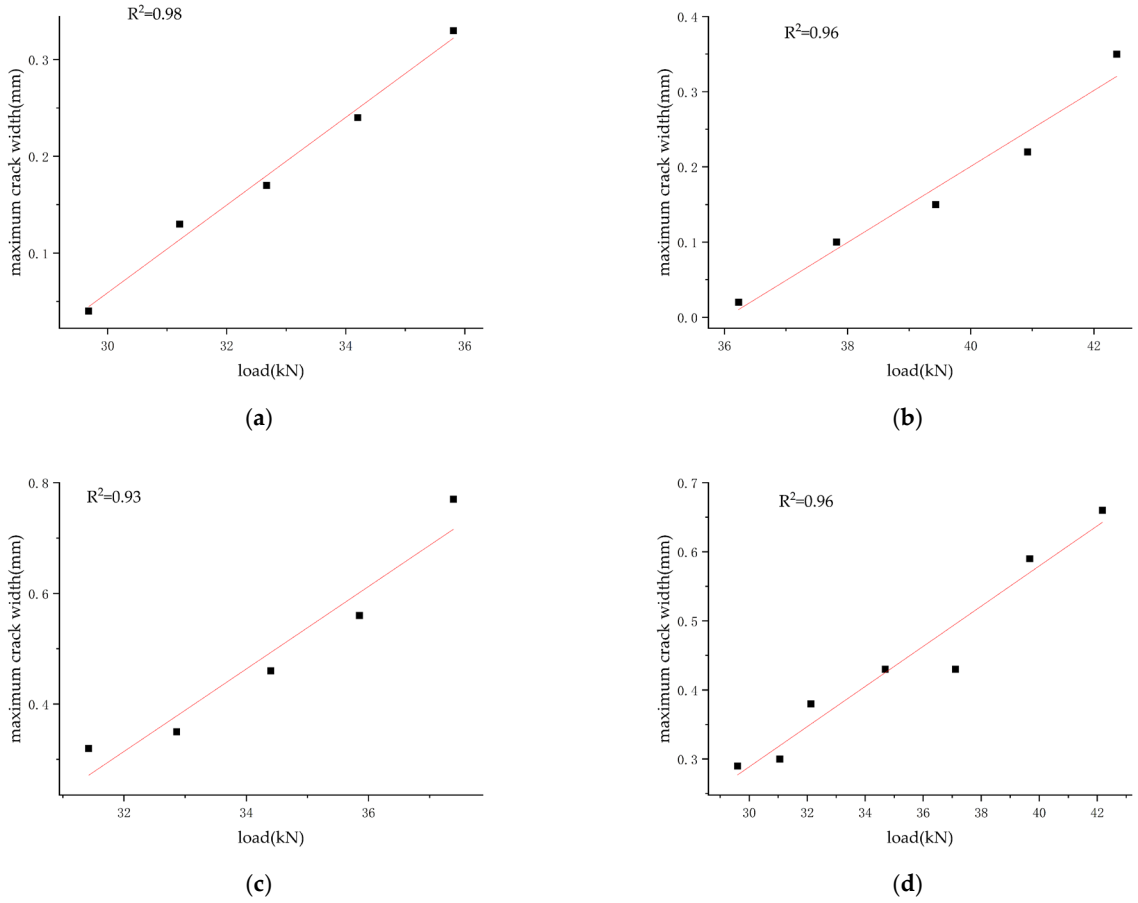

Figure 11. Relationship between external pressure load and the maximum crack width of the pipe (**a**) D1-B28-0-1; (**b**) D1-B28-1-2; (**c**) D1-C28-0-2; (**d**) D1-C28-1-2.

Further comparisons indicate the following:

1. The reinforcement type has a pronounced influence on crack control. In general, steel bars have a higher elastic modulus, enabling the post-cracking section to better maintain stiffness in the tension zone and thereby resulting in a relatively moderate increase in crack width. In contrast, GFRP bars have a lower elastic modulus, leading to more pronounced post-cracking stiffness degradation. Under the same load increment, larger tensile strains and crack openings are therefore more likely to occur. As a result, the GFRP-reinforced specimens tend to exhibit a larger fitted parameter, indicating a higher sensitivity of crack development to the applied load.
2. The addition of short fibers inhibits post-cracking crack propagation. Short fibers share part of the tensile stress through bridging, delay crack-tip propagation, and enhance crack-growth resistance, thereby promoting a transition from "rapid propagation" to "stable propagation." This effect helps reduce the crack-propagation rate and improves the stability of crack control. The fiber-reinforced specimens shown in Figure 11 also exhibit good linearity, indicating that the fibers primarily modify the post-cracking crack-growth slope and load-carrying interval, rather than the linear evolution characteristic during the stable propagation stage.

In summary, during the stable post-cracking stage under external pressure, the evolution of the maximum crack width can be well characterized by a linear fitting relationship, with high fitting accuracy for all specimens (all $R^2 > 0.93$). The linear fitting parameter can therefore be used as a key index for evaluating the crack-control performance of different reinforcement types and fiber contents: the smaller its value, the slower the crack propagation and the stronger the crack-control capacity.

5. Conclusions

1. Single-filament pull-out tests showed an approximately linear relationship between the pull-out force of rGFRP short fibers and effective embedded length, based on which an empirical embedded length-pull out force model was established. Combined with Monte Carlo simulation of randomness in fiber spatial distribution, orientation, and embedded length, the resultant fiber-bridging force and its moment contribution at the cracked section can be quantified, thereby explicitly introducing crack width—a key serviceability indicator—into the capacity calculation.
2. Test results show that adding 1% (by volume) rGFRP short fibers significantly improves crack resistance and load-carrying capacity: the cracking load increases by about 11.81% on average, and the ultimate load increases by about 0.45% on average. Fiber addition delays crack coalescence and propagation and improves the stability and ductility of the failure process.
3. Replacing steel bars with equal-area GFRP bars provides only a limited increase in cracking load for large-diameter specimens (Series D1, on average 1.35%), but substantially reduces ultimate load (on average 35.45%). This difference mainly arises because the lower elastic modulus of GFRP bars causes faster post-cracking stiffness degradation and more sensitive crack development, which drives the compression zone into crushing control at an earlier stage.
4. The predicted cracking and ultimate loads agree well with measurements overall, with an average absolute error of 14.37%, confirming the model's predictive capability within an engineering-acceptable range. In addition, in the post-cracking stage, external pressure load and maximum crack width exhibit a strong linear correlation ($R^2 > 0.93$); the linear fitting parameters can serve as key indicators for comparing crack-control effectiveness under different reinforcement types and fiber dosages.

In summary, this study introduces a crack-width-dependent characterization method for rGFRP short-fiber bridging, refines the load-carrying capacity calculation method for reinforced concrete pipes incorporating rGFRP short fibers, and verifies its effectiveness experimentally. This work can provide rGFRP short fibers and GFRP bar-reinforced concrete pipes under TEB loading for load-carrying capacity prediction and crack-control design, supported by calculation procedures and experimental data.

Author Contributions: Conceptualization, J.C.; Methodology, S.W., M.S. and Y.L.; Investigation, S.W. and P.S.; Data Curation, S.W.; Writing—Original Draft, S.W.; Writing—Review and Editing, J.C.; Funding Acquisition, J.C. All authors have read and agreed to the published version of the manuscript.

Funding: This work was supported by Zaoqiang County Bureau of Industry and Information Technology under Grant No. 20231g0058.

Data Availability Statement: The data supporting the findings of this study are available within the article.

Acknowledgments: The authors would like to thank Hengrun New Materials Group Co., Ltd. for its assistance with the experimental work.

Conflicts of Interest: Author Pengfei Song is affiliated with Hengrun New Materials Group Co., Ltd. The company assisted with the experimental work but had no influence on the other parts of the study. The authors declare no other conflicts of interest.

Abbreviations

The following abbreviations are used in this manuscript:

FRP	Fiber-Reinforced Polymer
rGFRP	recycled Glass Fiber-Reinforced Polymer

GFRP	Glass Fiber-Reinforced Polymer
TEB	Three-Edge Bearing

References

1. Benzeguir, Z.E.A.; Chaallal, O. Size Effect in FRP Shear-Strengthened RC Beams: Design Models versus Experimental Data. *CivilEng* **2021**, *2*, 874–894. [CrossRef]
2. Oliveux, G.; Dandy, L.O.; Leeke, G.A. Current Status of Recycling of Fibre Reinforced Polymers: Review of Technologies, Reuse and Resulting Properties. *Prog. Mater. Sci.* **2015**, *72*, 61–99. [CrossRef]
3. Pickering, S.J. Recycling Technologies for Thermoset Composite Materials—Current Status. *Compos. Part A Appl. Sci. Manuf.* **2006**, *37*, 1206–1215. [CrossRef]
4. Gao, F.F.; Duan, S.Y.; Wang, W.D.; Shi, Y.-L. Mechanical Properties and Microscopic Mechanism of Concrete Incorporation of Recycled GFRP Fiber with Different Sizes Recovered from Ex-Service Wind Turbine Blades. *Constr. Build. Mater.* **2025**, *491*, 142833. [CrossRef]
5. Jeswani, H.; Krüger, C.; Russ, M.; Horlacher, M.; Antony, F.; Hann, S.; Azapagic, A. Life Cycle Environmental Impacts of Chemical Recycling via Pyrolysis of Mixed Plastic Waste in Comparison with Mechanical Recycling and Energy Recovery. *Sci. Total Environ.* **2021**, *769*, 144483. [CrossRef] [PubMed]
6. Gonçalves, R.M.; Martinho, A.; Oliveira, J.P. Recycling of Reinforced Glass Fibers Waste: Current Status. *Materials* **2022**, *15*, 1596. [CrossRef]
7. Tao, Y.; Hadigheh, S.A.; Wei, Y. Recycling of Glass Fibre Reinforced Polymer (GFRP) Composite Wastes in Concrete: A Critical Review and Cost Benefit Analysis. *Structures* **2023**, *53*, 1540–1556. [CrossRef]
8. Brazão Farinha, C.; De Brito, J.; Veiga, R. Assessment of Glass Fibre Reinforced Polymer Waste Reuse as Filler in Mortars. *J. Clean. Prod.* **2019**, *210*, 1579–1594. [CrossRef]
9. Zhou, B.; Zhang, M.; Wang, L.; Ma, G. Experimental Study on Mechanical Property and Microstructure of Cement Mortar Reinforced with Elaborately Recycled GFRP Fiber. *Cem. Concr. Compos.* **2021**, *117*, 103908. [CrossRef]
10. Bu, Z.; Zhou, M.; Chao, H.; Chen, J.; Ouyang, X.; Yang, X.; Che, D.; Guo, Y.; Ma, Y. Multiscale Study on the Effect of Recycled Glass Fiber on the Rheological, Hydration, and Mechanical Properties of Cement Paste. *Constr. Build. Mater.* **2025**, *472*, 140932. [CrossRef]
11. Ribeiro, M.C.S.; Fiúza, A.; Ferreira, A.; Dinis, M.D.L.; Castro, A.C.M.; Meixedo, J.P.; Alvim, M.R. Recycling Approach towards Sustainability Advance of Composite Materials' Industry. *Recycling* **2016**, *1*, 178–193. [CrossRef]
12. Asokan, P.; Osmani, M.; Price, A.D.F. Improvement of the Mechanical Properties of Glass Fiber Reinforced Plastic Waste Powder Filled Concrete. *Constr. Build. Mater.* **2010**, *24*, 448–460. [CrossRef]
13. García, D.; Vegas, I.; Cacho, I. Mechanical Recycling of GFRP Waste as Short-Fiber Reinforcements in Microconcrete. *Constr. Build. Mater.* **2014**, *64*, 293–300. [CrossRef]
14. Ogi, K.; Shinoda, T.; Mizui, M. Strength in Concrete Reinforced with Recycled CFRP Pieces. *Compos. Part A Appl. Sci. Manuf.* **2005**, *36*, 893–902. [CrossRef]
15. Tittarelli, F.; Moriconi, G. Use of GRP Industrial By-Products in Cement Based Composites. *Cem. Concr. Compos.* **2010**, *32*, 219–225. [CrossRef]
16. Correia, J.R.; Almeida, N.M.; Figueira, J.R. Recycling of FRP Composites: Reusing Fine GFRP Waste in Concrete Mixtures. *J. Clean. Prod.* **2011**, *19*, 1745–1753. [CrossRef]
17. Baturkin, D.; Hisseine, O.A.; Masmoudi, R.; Tagnit-Hamou, A.; Massicotte, L. Valorization of Recycled FRP Materials from Wind Turbine Blades in Concrete. *Resour. Conserv. Recycl.* **2021**, *174*, 105807. [CrossRef]
18. Yazdanbakhsh, A.; Bank, L.C.; Rieder, K.-A.; Tian, Y.; Chen, C. Concrete with Discrete Slender Elements from Mechanically Recycled Wind Turbine Blades. *Resour. Conserv. Recycl.* **2018**, *128*, 11–21. [CrossRef]
19. Yazdanbakhsh, A.; Bank, L.C.; Tian, Y. Mechanical Processing of GFRP Waste into Large-Sized Pieces for Use in Concrete. *Recycling* **2018**, *3*, 8. [CrossRef]
20. Sheikh, S.A.; Kharal, Z. Replacement of Steel with GFRP for Sustainable Reinforced Concrete. *Constr. Build. Mater.* **2018**, *160*, 767–774. [CrossRef]
21. Shabani, H.; Asadian, A.; Galal, K. Flexural and Serviceability Behaviour of Macro-Synthetic Fibre-Reinforced Concrete Beams Reinforced with GFRP Bars. *Constr. Build. Mater.* **2025**, *494*, 143217. [CrossRef]
22. Bui, L.; Stitmannaithum, B.; Ueda, T. Mechanical Performances of Concrete Beams with Hybrid Usage of Steel and FRP Tension Reinforcement. *Comput. Concr.* **2017**, *20*, 391–407. [CrossRef]
23. Sun, Z.; Yang, Y.; Yan, W.; Wu, G.; He, X. Moment-Curvature Behaviors of Concrete Beams Singly Reinforced by Steel-FRP Composite Bars. *Adv. Civ. Eng.* **2017**, *2017*, 1309629. [CrossRef]
24. Sun, Z.Y.; Yang, Y.; Qin, W.H.; Ren, S.; Wu, G. Experimental Study on Flexural Behavior of Concrete Beams Reinforced by Steel-Fiber Reinforced Polymer Composite Bars. *J. Reinf. Plast. Compos.* **2012**, *31*, 1737–1745. [CrossRef]

25. Harajli, M.H.; Abouniaj, M. Bond Performance of GFRP Bars in Tension: Experimental Evaluation and Assessment of ACI 440 Guidelines. *J. Compos. Constr.* **2010**, *14*, 659–668. [CrossRef]
26. Saikia, B.; Kumar, P.; Thomas, J.; Rao, K.S.N.; Ramaswamy, A. Strength and Serviceability Performance of Beams Reinforced with GFRP Bars in Flexure. *Constr. Build. Mater.* **2007**, *21*, 1709–1719. [CrossRef]
27. Tavares, D.H.; Giongo, J.S.; Paultre, P. Behavior of Reinforced Concrete Beams Reinforced with GFRP Bars. *IBRACON Struct. Mater. J.* **2008**, *1*, 285–295. [CrossRef]
28. El-Nemr, A.; Ahmed, E.A.; Benmokrane, B. Flexural Behavior and Serviceability of Normal- and High-Strength Concrete Beams Reinforced with Glass Fiber-Reinforced Polymer Bars. *ACI Struct. J.* **2013**, *110*, 1077–1088. [CrossRef]
29. Haktanir, T.; Ari, K.; Altun, F.; Karahan, O. A Comparative Experimental Investigation of Concrete, Reinforced-Concrete and Steel-Fibre Concrete Pipes under Three-Edge-Bearing Test. *Constr. Build. Mater.* **2007**, *21*, 1702–1708. [CrossRef]
30. Wilson, A.; Abolmaali, A. Performance of Synthetic Fiber-Reinforced Concrete Pipes. *J. Pipeline Syst. Eng. Pract.* **2014**, *5*, 04014008. [CrossRef]
31. Lee, S.; Park, Y.; Abulemal, A. Investigation of Flexural Toughness for Steel- and Synthetic-Fiber-Reinforced Concrete Pipes. *Structures* **2019**, *19*, 203–211. [CrossRef]
32. *ASTM C497/C497M-25*; Standard Test Methods for Concrete Pipe, Concrete Box Sections, Manhole Sections, or Tile. ASTM International: West Conshohocken, PA, USA, 2025.
33. *GB/T 11836-2023*; Concrete and Reinforced Concrete Drainage Pipes. China Standards Press: Beijing, China, 2023.
34. Zhang, X. Theoretical and Numerical Study on the Three-Edge Bearing Capacity of Prestressed Concrete Cylinder Pipe. *KSCE J. Civ. Eng.* **2022**, *26*, 1254–1266. [CrossRef]
35. ACI Committee 318. *Building Code Requirements for Structural Concrete (ACI 318-19) and Commentary (ACI 318R-19)*; American Concrete Institute: Farmington Hills, MI, USA, 2019.
36. Zhao, T.; Song, P.; Dong, G.; Lv, Y.; Sun, M.; Chen, J. Experimental Research and Theoretical Prediction on Mechanical Properties for Recycled GFRP Fiber Reinforced Concrete. *J. Build. Eng.* **2024**, *91*, 109643. [CrossRef]